مها

REPORT DOCUMENTATION PAGE

Form Approved
OMB No. 0704-0188

Public gathe collec Davis

1. A

AD-A245 011



ge 1 hour per response, including the time for reviewing instructions, searching existing data sources, collection of information. Send comments regarding this burden estimate or any other aspect of this ashington Headquarters Services, Directorate for Information Operations and Budget, Paperwork Reduction Project (0704-0188), Washington, DC 20503.

3. REPORT TYPE AND DATES COVERED REPLIED

4. TITLE AND SUBTITLE

Title shown on Reprint

5. FUNDING NUMBERS

DAAL 03-90-C-0013

6. AUTHOR(S)

Author(s) listed on Reprint

8. PERFORMING ORGANIZATION

REPORT NUMBER

7. PERFORMING ORGANIZATION NAME(S) AND ADDRESS(ES)

JAI associates, Inc.

Moffett field, CA 94035-1000

9. SPONSORING/MONITORING AGENCY NAME(S) AND ADDRESS(ES)

U. S. Army Research Office

P. O. Box 12211

Research Triangle Park, NC 27709-2211

10. SPONSORING / MONITORING AGENCY REPORT NUMBER

ARO 27752.2-EG

11. SUPPLEMENTARY NOTES

The view, opinions and/or findings contained in this report are those of the author(s) and should not be construed as an official Department of the Army position, policy, or decision, unless so designated by other documentation.

12a. DISTRIBUTION / AVAILABILITY STATEMENT

12b. DISTRIBUTION CODE

Approved for public release; distribution unlimited.

13. ABSTRACT (Maximum 200 words)

ABSTRACT ON REPRINT

S DTIC S ELECTE JAN 1 0 1992

14. SUBJECT TERMS

15. NUMBER OF PAGES

16. PRICE CODE

UL

17. SECURITY CLASSIFICATION OF REPORT

18. SECURITY CLASSIFICATION
OF THIS PAGE
UNCLASSIFIED

19. SECURITY CLASSIFICATION OF ABSTRACT

20. LIMITATION OF ABSTRACT

UNCLASSIFIED

UNCLASSIFIED

FLOWFIELD ANALYSIS OF MODERN HELICOPTER ROTORS IN HOVER BY NAVIER-STOKES METHOD

G. R. Srinivasan

JAI Associates, Inc.

NASA Ames Research Center, Moffett Field, CA 94035, U.S.A.

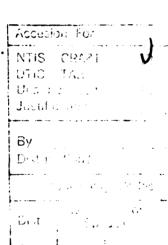
V. Raghavan

Sterling Federal Systems

NASA Ames Research Center, Moffett Field, CA 94035, U.S.A.



U.S. Army Aeroflightdynamics Directorate - AVSCOM NASA Ames Research Center, Moffett Field, CA 94035, U.S.A.





INTERNATIONAL TECHNICAL SPECIALISTS MEETING

Rotorcraft Acoustics and Rotor Fluid Dynamics

October 15-17, 1991 Philadelphia, Pennsylvania, USA

02 1 m 3 20

FLOWFIELD ANALYSIS OF MODERN HELICOPTER ROTORS IN HOVER BY NAVIER-STOKES METHOD

G. R. Srinivasan

JAI Associates Inc.

NASA Ames Research Center, Moffett Field, California 94035, USA

V. Raghavan

Sterling Federal Systems

NASA Ames Research Center, Moffett Field, California 94035, USA

E. P. N. Duque

U. S. Army Aeroflightdynamics Directorate -AVSCOM NASA Ames Research Center, Moffett Field, California 94035, USA

Abstract

The viscous, three-dimensional, flowfields of UH60 and BERP rotors are calculated for lifting hover configurations using a Navier-Stokes computational fluid dynamics method with a view to understand the importance of planform effects on the airloads. In this method, the induced effects of the wake, including the interaction of tip vortices with successive blades, are captured as a part of the overall flowfield solution without prescribing any wake models. Numerical results in the form of surface pressures, hover performance parameters, surface skin friction and tip vortex patterns, and vortex wake trajectory are presented at two thrust conditions for UH60 and BERP rotors. Comparison of results for the UH60 model rotor show good agreement with experiments at moderate thrust conditions. Comparison of results with equivalent rectangular UH60 blade and BERP blade indicates that the BERP blade, with an unconventional planform, gives more thrust at the cost of more power and a reduced Figure of Merit. The high thrust conditions considered produce severe shock-induced flow separation for UH60 blade, while the BERP blade develops more thrust and minimal separation. The BERP blade produces a tighter tip vortex structure compared with the UH60 blade. These results and the discussion presented bring out the similarities and differences between the two rotors.

Nomenclature

| a_{∞} | = | speed of sound, characteristic velocity | | |
|--------------|---|---|--|--|
| ь | = | number of blades | | |
| c(r) | = | blade chord at radial location r | | |

| c_{eq} | = | equivalent blade chord, $1/R \int c(r)dr$ |
|---|-----|--|
| c_{tw} | = | thrust-weighted equivalent chord, |
| | | $\int c(r)r^2dr/\int r^2dr$ |
| C_p | = | pressure coefficient based on local |
| ŕ | | dynamic pressure |
| $C_{m{Q}}$ | = | rotor torque coefficient, $Q/(2q(R)\pi R^3)$ |
| C_t | = | sectional thrust coefficient based on |
| | | local chord, $dt/dr/(c(r)q(R))$ |
| \overline{C}_t | = | sectional thrust coefficient based on |
| | | $c_{eq}, dt/dr/(c_{eq}q(R))$ |
| C_{tave} | = | area under Ct vs r curve |
| \overline{C}_{tave} | = | area under \overline{C}_t vs r curve |
| C_T | = | rotor thrust coefficient, $T/(2q(R)\pi R^2)$ |
| e | = | energy per unit volume |
| $\stackrel{e}{\widehat{E}}, \widehat{F}, \widehat{C}$ | }= | flux vectors |
| FM | = | Figure of Merit, $0.707C_T^{3/2}/C_Q$ |
| M_{tip} | = | blade tip Mach number |
| q(R) | = | rotational dynamic pressure, |
| | | $1/2 \rho(\Omega R)^2$ |
| $egin{array}{c} \widehat{Q} \ Q \end{array}$ | = | flow-field vector |
| Q | = | rotor torque |
| r R | = | rotor radial coordinate |
| | = | blade radius |
| Re | = | Reynolds number based on M_{tip} and |
| | | Ceq |
| $\widehat{\mathcal{S}}$ | = | viscous flux vector |
| T | = | rotor thrust |
| u, v, w | = | velocity components in physical space |
| u_{loc} | = | local blade speed |
| x, y, z, | t = | physical space coordinates |
| α | = | angle of attack, degrees |
| r Î | = | sectional circulation |
| $\widehat{\Gamma}$ | = | normalised blade sectional circulation, |
| | | $\Gamma/\Omega R^2$ |
| \mathcal{I}_{c} | = | collective pitch |
| | | |

Presented at the International Technical Specialists Meeting on Rotorcraft Acoustics and Rotor Fluid Dynamics, Philadelphia, PA, October 15-17, 1991.

ho = density σ = rotor geometric solidity, $b \int c(r)rdr/(\pi R^2)$ σ_T = rotor thrust-weighted solidity, $b \int c_{tw}rdr/(\pi R^2)$ ξ, η, ζ, τ = generalized curvilinear coordinates Ω = rotor angular velocity

Introduction

The accurate prediction of the flowfield of a helicopter rotor continues to be one of the most complex and challenging problems in applied aerodynamics. This is true despite the availability of the present day supercomputers of Cray-2 class and improved numerical algorithms. The complexity of the flow stems from several peculiar features that are unique to a helicopter rotor; the dominant of these is the vortical wake, which strongly influences the operating characteristics. Accurate prediction of this vortical wake is probably the most important, most studied and the most difficult aspect of helicopter flowfield.

Current methods of analysis of wakes range in complexity from relatively simple momentum-theory applications to sophisticated free-wake methods. In between these extremes, there exists a variety of so-called prescribed-wake models¹. Although such methods are often used in industry for predicting airloads, they do suffer from the limitation that the empirical determination of wake shape ignores some of the important flowfield details such as the mutual interaction of individual vortex elements. The fact that most of these methods have to be coupled with some wake model, for realistic estimates of airloads, restrict their application to blade shapes and planforms that are geometrically simple. Besides, further modeling is required to simulate the formation of concentrated tip vortex in the tip region.

The recent application of Computational Fluid Dynamics (CFD) methods to predict these complex flows has opened a new avenue to address these problems more rigorously. Methods based on the solutions of full-potential, the Euler and the Navier-Stokes equations abound in the literature. Although most of these methods still use some sort of wake model to bring-in the influence of vortical wake, there are methods that capture the effects of wake fairly accurately as a part of the overall flowfield. In this regard, the recent methods based on the solutions of full-potential², the Euler^{3,4} and the Navier-Stokes⁵ equations are noteworthy.

In the present study, the Navier-Stokes methodology of Srinivasan et al.5 is used to calculate the flowfields of realistic helicopter rotor configurations of the UH60⁶ and BERP⁷ rotors for lifting hover configurations, with a view toward assessing the importance of planform effects on the airloads. Calculations are also performed for equivalent rectangular blade of the UH60 rotor to further understand the role of planform in determining the airloads and tip vortex wake geometry. The numerical code of Ref. 5, called TURNS (Transonic Unsteady Rotor Navier-Stokes), will be utilized for this purpose. This methodology has been validated with experimental data for aerodynamics and aeroacoustics of high-speed impulsive noise for rotors in hover and forward flight⁸. Currently the vortical structure calculated with this method is smeared due to grid coarseness. However, the nearfield wake trajectory is captured fairly accurately. The use of the Navier-Stokes method enhances (a) the tip flow simulation which involves resolving the three-dimensional separated flow and concentrated tip vortex, and (b) the accurate simulation of strong viscous-inviscid interaction involving shock-induced separation at high blade tip speeds.

Govering Equations and Solution Methodology

The governing partial differential equations are the unsteady, thin-layer Navier-Stokes equations. For generality, these equations are written in strong conservation-law form in gereralized body-conforming curvilinear space (ξ, η, ζ, τ) and are given by

$$\partial_{\tau}\widehat{Q} + \partial_{\xi}\widehat{E} + \partial_{\eta}\widehat{F} + \partial_{\zeta}\widehat{G} = Re^{-1}\partial_{\zeta}\widehat{S} \tag{1}$$

where

$$Q = [\rho, \rho u, \rho v, \rho w, e]^{T}, \widehat{Q} = Q/J$$
 (2)

is the flowfield vector being solved for and \widehat{E} , \widehat{F} , \widehat{G} are convective flux vectors and \widehat{S} is the viscous flux vector being considered in the thin layer limit; J is the Jacobian of transformation, Re is the Reynolds number and the sign indicates that the quantity is normalized by the Jacobian. The primitive variables of Eq. (1) are the density ρ , the three mass fluxes ρu , ρv and ρw in the three coordinate directions x, y and z, respectively and the energy per unit volume e. All these quantities are nondimensionlized by the appropriate free stream reference quantities. The chord of the rotor blade and the free stream sound speed are assumed to be the characteristic length and velocity scales. The equation set given by Eq. (1) together with the equation of state for a perfect gas describe the entire flowfield.

The finite-difference implicit numerical scheme for the solution of Eq. (1) is described in Ref. 5. Briefly, the numerical algorithm uses a Roe upwind-biased scheme for all three coordinate directions with higherorder MUSCL-type limiting for the right-hand side to model shocks and for propagating acoustics accurately. The use of Roe's upwinding eliminates the addition of explicit dissipation and thus produces a less dissipative numerical scheme. The LU-SGS (lower-upper symmetric Gauss-Seidel) implicit operator used for the lefthand side makes the numerical scheme computationally efficient as well as robust. The option of Newton subiterations at each time-step reduces the linearization and factorization errors as well as makes the numerical scheme second-order accurate in time. This is particulary useful for unsteady calculations (forward flight). Currently the scheme is third-order accurate in space and first- or second-order accurate in time.

To take advantage of the quasi-steady nature of the hovering rotor flowfield, the governing equations are solved in the blade-fixed coordinate system. This necessitates addition of source terms to account for the centrifugal force of rotation of the blades. The coordinate transformation space metrics are evaluated using a finite volume formulation. Although such a method captures free-stream accurately, formation of time metrics rigorously with this scheme is computationally expensive. So, a finite-difference formulation is adopted for unsteady metrics. Further, a locally-varying timestep is used in the integration procedure to accelerate convergence¹⁰ of numerical scheme. With these features, the code is robust, fairly efficient, and runs at 140 MFLOPS on a Cray Y-MP supercomputer.

Body conforming finite-difference grids are used for the long slender blades of the UH60 and Lynx BERP rotors. These blades, shown in planform in Fig. 1, have aspect ratios of 15.51 and 12.46 respectively. The e are highly twisted and have a twist distribution alona their lengths as shown in Fig. 2. The characteristics of UH60 blade is that it has a hook-like twist distribution in the tip region with a swept-back planform in this area. The chord of the blade is constant along its entire length with a rectangular planform except in the swept-back part of the blade. The BERP blade on the other hand, has a large paddle-type planform in the outer part of the blade near the tip. The twist change is linear like the UH60 blade up until the paddle part where it decreases to a negative constant value.

Because of the axial symmetry of the hovering rotor flowfield, a C-H grid topology is chosen with C-type in

the chordwise direction and H-type in the spanwise direction. The H-type spanwise topology creates a bevel tip for the square-tipped UH60 blades. To adapt to the cylindrical flowfield of the rotor, three-dimensional grids are constructed for these blades by stacking and bending two-dimensional C-H grids so that they lie on the blade along the chord. Typical fine grids have nearly 940,000 points with 217 points in the chordwise direction and 71 and 61 points in the spanwise and normal directions, respectively. These grids have clustering in the leading and trailing edge regions as well as in the tip region. The grid lines are nearly orthogonal at the surface with a spacing of 0.00004 chord in the normal direction. The grid boundary is located at two rotor diameters at the top and bottom boundaries and one radius beyond the tip in the spanwise direction. Coarse grids have been constructed by eliminating every other point in all three-directions and typically have 120,000 points. Figure 3 shows the views these grids (for single blades) in the plane of the blades. Figure 4 shows a view of a grid for single blade constructed for BERP blade. This typical grid shows the grid boundaries and the details of grid clustering near the grid surface and in the tip region.

The boundary conditions are applied explicitly. At the surface a noslip condition is used, but the surface will have finite velocity due to the blade rotation introduced through the time metrics. Characteristic-type boundary conditions are used at the farfield; this point is discussed in more detail later in the paper. The surface pressure is determined by solving the normal momentum equation and the density is evaluated by the adiabatic wall condition. At the inboard-plane boundary, near the axis of rotation of the blade, the flow quantities are extrapolated from the grid interior. For a hovering rotor with identical blades, the flow associated with each blade is assumed to be the same. To take advantage of this situation, only the flowfield of a single blade is calculated by bringing information of neighboring blades through periodic boundaries4 shown in Fig. 4. The flow of the entire rotor is then assembled through a post-processing procedure by combining the flowfields of individual blades. Finally, the calculations reported here assume fully turbulent flow for the blades and laminar flow in the wake. The simple algebraic turbulence model of Baldwin and Lomax¹¹ is used to estimate the eddy viscosity.

Results

The present numerical scheme with its wakecapture feature has performed better in resolving the tip flow, shocks and overall airloads than many Navier-Stokes methods that have used wake models or some variance of such models^{12,13}. In contrast to the the model two-bladed hovering rotor¹⁴ considered for calculations with this solution method in a previous study⁵, the present study considers four-bladed model UH60 rotor and actual BERP rotor. The blades of these rotors, as previously noted, have large aspect ratio and are highly twisted along their lengths (see Fig. 2). In addition they have non-rectangular planforms. As before⁵, the calculations are performed on isolated rotor blades and composite solutions are assembled by combining the flowfields of all four blades. In the calculation procedure, the evolution of the flowfield to a quasi-steady state is monitored as the blade is set in motion from a quiescent flow condition. Typical numerical results presented consists of surface pressures, sectional thrust distributions, surface oil flow patterns, tip vortex details, and wake trajectory.

UH60 Blackhawk Rotor

Figure 5 show typical plots of surface pressure distributions for the model UH60 blade at several radial stations. Although model hover tests are performed for this configuration and some plots of the experimental data are published⁶ for this rotor, much of the experimental information remains restricted. In view of this, a representative tip speed $(M_{tip} = 0.628)$ and thrust condition $(C_T/\sigma = 0.085)$ were selected and several collective pitch settings (θ_c) were tried out to match with experimental data. Results for $\theta_c = 9^{\circ}$ showed the closest match with experimental surface pressures. Figure 5 shows the comparison of these results with experiments. The numerical results appear to be in general agreement with the data at all span stations. The calculated $C_T/\sigma = 0.084$ for this case is also in good agreement with the experimental value of 0.085.

In order to assess the importance of planform effects, flowfield calculations were made on an equivalent rectangular blade of identical twist distribution as the UH60 blade (shown as Twist1 in Fig. 2) for the above flow conditions of $M_{tip} = 0.628$, and $\theta_c = 9^\circ$ and Re = 2.75×10^6 . The results are compared with the UH60 blade in Fig. 6 in a plot of sectional thrust coefficient (C_t) variation along the blade radius (r/R). In order to compare these results with experimental data⁶, the sectional thrust coefficient has been normalized by C_{tave} which is the area under the curve of C_t vs r/R. Since the equivalent rectangular blade has identical twist ditribution as the UH60 blade along its radius and has an unswept planform in the tip region, the differences seen with UH60 blade in Fig. 6 are only in this region. Although both these blades have bevelled tips (because of H-grid topology), the UH60 blade produces a relatively smaller separation in this region

than the equivalent rectangular blade (with unswept tip). The tip vortex location for the UH60 biade is slightly inboard of that seen for the equivalent rectangular blade. This observation is in general agreement with some previous studies of swept and unswept planforms with bevel-tips¹⁵. In terms of performance, the equivalent rectangular blade produces about 8% less thrust than the UH60 blade, and the Figure of Merit is lower. Table 1 details the performance parameters for these rotors.

Figure 7 shows the sectional thrust distribution along the radius of UH60 blade for two thrust conditions corresponding to $\theta_c = 9^{\circ}$ and 13° at $M_{tip} =$ 0.628 and Re = 2.75×10^6 . The high thrust condition of $\theta_c = 13^{\circ}$ produces a bound circulation distribution that gives 67% more thrust than the $\theta_c = 9^{\circ}$ case. The power requirement increases by a factor of 115%. It also produces a much stronger tip vortex which is located more inboard than the $\theta_c = 9^{\circ}$ case. The flow topology is very complicated on the blade for this high thrust condition with shock-induced boundary layer separation occurring over a large part of the blade, as shown by the surface particle tracers (skin friction lines) in Fig. 8. In contrast, as seen in the close-up view of the tip in Fig. 9, the low thrust case ($\theta_c = 9^{\circ}$) does not produce shock-induced flow separation. Both thrust conditions produce flow separation on the inboard parts of the blade as seen in Fig.8, but the spanwise extent is, of course, greater at $\theta_c = 13^{\circ}$. Figure 10 shows the extent of supercritical flow on the upper surface of the blade in the Mach number contours picture for the $\theta_c = 13^{\circ}$ case. Also shown in this figure are the Mach contours in a plane at r/R = 0.94. This shows the location of shock wave in the leading edge region, and the extent of supersonic pocket.

Two representative performance curves of the model UH60 rotor as calculated here for $M_{tip}=0.628$ are shown in Fig. 11 and Fig. 12 along with UTRC data⁶. The details of calculated results are shown in Table 1. In presenting these results, two observations have been made. First, the moderate thrust condition results are in good agreement with experimental data. Second, the high thrust condition considered in this study is apparently beyond the model test range. The calculated Figure of Merit is approximately the same at $\theta_c=13^\circ$ as at $\theta_c=9^\circ$ indicating that the rotor hover performance seems to stay relatively uniform for this rotor, at least over this range of θ_c .

In addition to the planform change study for this blade, a fictitious UH60 blade having the same planform, but with linear twist in the tip region (Twist2 in Fig. 2), instead of a hook-type of twist (Twist 1), was

considered to examine the importance of twist in this region on airloads. The sectional thrust distribution for this blade is shown in Fig. 6 along with results for the standard UH60 blade at the same test conditions as of Fig. 5. As seen in this figure, the blade generates lower thrust inboard (perhaps due to the slightly lower values of twist in this region), higher thrust at $r/R \simeq 0.8$ and lower thrust at the tip, compared to the UH60 blade. Overall, this blade produces 15% less thrust than the UH60 blade, and the Figure of Merit is significantly less. As before, there is no flow separation on the blade except in the very tip region. The tip vortex location is slightly inboard of the UH60 blade and has less tight braiding than the UH60 blade at a comparable blade location although this blade also has a swept-tip planform.

BERP Rotor

The BERP blade has an unorthodox planform 160shape with a twist distribution along its length as shown in Fig. 2. The details of the blade geometry is described elsewhere (see, for example, Ref. 7). The main feature of its geometry is a leading edge notch (see Fig. 1) associated with a paddle-type shape with increased chord and swept delta-wing-like planform in the tip region. This unusual planform and high performance airfoils have enabled BERP rotor to achieve high performance in high speed forward flight. In order to compare planform effects of this blade with UH60 blade, two calculations are made for collective pitch of $\theta_c = 9^{\circ}$ and 13° at a tip speed of $M_{tip} = 0.628$ and Re = 2.95 x 10⁶.

Figure 13 shows typical surface pressure for the BERP rotor at different radial locations for the flow condition corresponding to $\theta_c = 13^{\circ}$. Currently no experimental data is available for these flow conditions. However, these results and the surface pressures for θ_c = 9° appear to be in good qualitative agreement with the nonrotating blade results of Ref. 7. The sectional thrust variation is shown for this blade for $\theta_c = 9^{\circ}$ in Fig. 14, along with UH60 results at identical collective pitch and flow conditions. Since BERP blade has variable chord along its radius in contrast to the UH60 blade, the sectional thrust curve for BERP blade has an unusual shape in the paddle part of the blade. If the results of Fig. 14 are recast in terms of equivalent chord, then these results for BERP blade will have the familiar form as shown in Fig. 15. As seen in this comparison, the combination of leading-edge notch and increased area of paddle part of BERP has produced an increased thrust for the blade for this region. Inboard, however, it produces relatively lesser thrust perhaps because of slightly lower twist in this region. For both

conditions considered, the BERP blade produces more thrust at the expense of significantly more power.

Table 1 summarizes important hover performance results for this rotor. Figures 16-17 show the sectional thrust and bound circulation distributions for BERP blade for $\theta_c = 9^{\circ}$ and 13° at $M_{tip} = 0.628$ and Re = 2.95 x 106. In essence, these two plots show the same quantity but looking in different ways. The high thrust condition produces 80% more thrust at the expense of 160% more power compared to the moderate thrust condition, corresponding to $\theta_c = 9^{\circ}$, at the same tip speed. While the curves of Figs. 15 and 16 have the same qualitative behavior as that of UH60 blade shown in Fig. 7, the bound circulation distribution, shown in Fig. 17, has the same qualitative behavior as the sectional lift distribution of nonrotating BERP blade⁷. Of particular significance is the distribution in the vicinity of the notch. As observed for a nonrotating blade from both the wind tunnel tests and calculations, the present calculations also show that the sectional thrust of the blade in this region first decreases and then increases for the condition of $\theta_c = 13^{\circ}$. In contrast, the moderate thrust condition results does not show this behavior.

The surface particle tracer pictures of BERP blade are shown in Fig. 18 for $\theta_c = 9^{\circ}$ and 13°. For both the thrust conditions, the flow stays attached on the paddle part of the blade. The high thrust condition corresponding to $\theta_c = 13^{\circ}$, however, produces a complicated flow structure in the notch region identified as vortical flow structure. In spite of the strong supercritical flow for this condition, as in UH60 blade at $\theta_c =$ 13°, the BERP blade produces relatively small extent of shock-induced flow separation only in the inboard of notch region as seen in Fig. 18. The details of pressure contours on the upper surface of the blade and at one spanwise location in this region, shown in Fig. 19, highlights the extent of transonic flow for this flow condition. In contrast, the UH60 blade produces a severe shock induced flow separation over a large part of the blade for this flow condition. This total absence of flow separation on the paddle part of the blade at transonic conditions has a favorable influence on the performance of the blade. In the tip region, the case of $\theta_c = 13^{\circ}$ has produced a larger extent of separation on the upper surface than the $\theta_c = 9^{\circ}$ case. Since these blades have very high inboard twists, both conditions produce severe flow separation. The extent of separation for the $\theta_c = 13^{\circ}$ case, shown in Fig. 20, is much more massive than the $\theta_c = 9^{\circ}$ case as for UH60 blade case.

Comparison of surface particle tracers details for the UH60 (Fig. 9) and BERP (Fig. 18) rotors in the outer part of the blades towards the tip indicate the following features. Since the blades have totally different planforms and twist distributions in this region, they produce very different flow patterns. The UH60 blade has a hook-like twist distribution in the swept part near the tip while the BERP blade has negative constant twist with a large paddle part and a delta-wing like tapered tip. For the low thrust case, corresponding to $\theta_c = 9^{\circ}$, both blades show completely attached flow except for the tip region. In contrast, at the high thrust condition ($\theta_c = 13^{\circ}$), they have totally different surface flow patterns. The UH60 blade shows strong shockinduced separation and reattachment near the leading edge area on other side of kink (begining of sweep-back position), whereas the BERP blade shows completely attached flow on the paddle-part except in the extreme tip region. The notch region has a complicated flow separation and vortical flow structure.

Figure 21 shows the details of a typical tip vortex formation and roll up process for the BERP blade. This type of flow visualization picture is generated by releasing unrestricted flow particle tracers in the tip region on both sides of the blade at different chordwise and spanwise locations and at different heights from the surface of the blade. The particles so released bunch-up and get braided over each other to form a distinct structure of concentrated vorticity. Such a structure represents the formation process of a concentrated tip vortex as seen in Fig. 21. As this tip vortex is still forming, it starts to roll-up and in the process stays distinctly above the wake vortex sheet. Once it leaves the surface, it convects with the wake. As this vortex wake convects, it contracts in size and descends with the flow. With the present nonadaptive, structured grids used, the captured vortex structure is smeared. This means the core is diffuse but the circulation is correctly captured in strength.

Comparing the vortical flow structures of UH60 and BERP blades corresponding to $\theta_c = 13^\circ$, both have distinct but diffuse tip vortex structures. The notch area of BERP produces a complex vortical stucture as seen in Fig. 21. Similary, the kink of UH60 blade also produces a very mild vortical structure for this condition. Comparison of tip vortex formation processes of UH60 blade and equivalent rectangular blade for the low thrust condition, corresponding to $\theta_c = 9^\circ$ case, indicates that the equivalent rectangular blade shows similar formation and roll-up process as that of UH60 blade except that the braiding of the particle tracers occurs much farther in the wake in conformity with the observations made in Ref. 15.

Farfield Boundary Conditions

A difficult aspect of numerical prediction of hovering rotor flows is the prescription of farfield boundary conditions. In hover, if the specification of farfield boundary conditions is based on the quiescent flow outside of the computational box, then the flow into and out of the box will be zero. This creates a closed box atmosphere for the rotor, with the flow inside the box recirculating when the rotor is spinning. In principle, this is precisely the environment in many hover test chambers. However, a large computational box of this size is not cost effective and exceeds the memory limits of present day supercomputers. Alternatively, with a smaller computational box around the rotor one should specify non-zero flow farfield boundary conditions that will allow the flow to enter and exit the box without violating the conservation laws. Currently, no precise methods are available to specify these boundary conditions, although some schemes have been suggested³. The present calculations take a slighty different approach to specifying farfield conditions. A three-dimensional sink whose strength is determined from the thrust of the rotor, is located at the axis of rotation in the plane of the rotor. With this, the flow enters the computational box from all boundaries, except through an exit plane on the lower boundary whose area is half the area of the rotor disk. Across this exit plane, a characteristic-type outflow boundary condition is specified by prescribing the w-velocity as twice its value at the rotor plane from the momentum theory concept. The other four quantities are extrapolated from within.

Using the above approach of specifying the farfield boundary conditions, calculations were repeated for the UH60 blade at flow conditions of $M_{tip}=0.628$, $\theta_c=9^\circ$ and $Re=2.75x10^6$. Figure 22 shows a typical result of sectional thrust distribution compared with that generated with old boundary conditions precedure and with experiments. Although there is general agreement of overall results in this plot, the reasons for small differences seen near the kink and in the tip region is not clear at this time. The performance parameters are shown in Table 1. As seen in this, the thrust and power values are about 3% more than that of the old boundary conditions.

The important test of this new boundary condition study is the behavior of the captured wake trajectory. After identifying the fluid particle tracers that reside with the core of the tip vortex, such as shown in Fig. 21, one or more fluid particle tracers were released in the tip region of each blade and the evolution of these tracers in time was monitored. Figure 23 shows two

views, a) contraction, and b) descent, of such a wake trajectory for the above test case. The nearfield trajectory of this wake, for both contraction and descent, appears to be in reasonable agreement with the experiments and is shown in Fig. 24. Previous calculations, for the same computational box with old boundary conditions, showed that the wake trajectory for this four-bladed rotor was accurately captured only up to about 180° of vortex age (azimuth travel). Subsequently, the wake trajectory continued to descend but expanded in size, from its previous size at 180° azimuth, and eventually got cought in the recirculating flow. With the new farfield boundary conditions, the flow exits smoothly at the bottom boundary and so does the wake.

Concluding Remarks

A limited airloads and flowfield analysis of the UH60 model rotor and the BERP rotor is presented for lifting hover configurations. The calculation procedure uses a computational fluid dynamics Navier-Stokes capability to capture the flowfield and nearfield vortical wake and its trajectory without having to prescribe any wake models. At present, the vortical structure in the wake is smeared due to grid coarseness, and this aspect of the method needs further improvements. Nevertheless, the induced flow in the plane of the rotor and the near-field wake trajectory are computed fairly accurately, and the calculated pressures on the blade agree well with experiments.

The results and discussion presented here focus on evaluating the importance and influence of planform effects on the airloads and vortex wake geometry. The results for the UH60 rotor show good agreement with experimental data for the surface pressures, thrust, power and fair agreement for wake trajectory. For a given flow condition, the BERP rotor produces more thrust at the expense of increased power and reduced Figure of Merit. The results for the UH60 and BERP blades at transonic high thrust conditions indicate that the BERP blade produces milder shock-induced separation than the UH60 blade. The BERP blade also shows tightly braided tip vortex structure compared to the UH60 blade. The good comparison of the UH60 rotor performace calculations with experiments indicates that this free-wake Navier-Stokes CFD capability is promising as a tool for analysing the properties of new and exotic blade shapes whose properties are not known a priori.

Acknowledgements

The authors would like to thank Dr. W. J. Mc-Croskey and Dr. C. Tung for their encouragement,

continued interest, and useful discussions. The first author (GRS) would like to acknowledge the support of his research by the U. S. Army Research Office under Contract DAAL03-90-C-0013. Computational time was provided by the NAS and the Applied Computational Fluids Branch of NASA Ames Research Center.

References

- 1. Caradonna, F. X. and Tung, C., "A Review of Current Finite Difference Rotor Flow Codes", Proceedings of the 42nd Annual Forum of the American Helicopter Society, Washington, D. C., June 1986, pp. 967-983.
- 2. Ramachandran, K., Tung, C. and Caradonna, F. X., "Rotor Hover Performance Prediction Using a Free-Wake Computational Fluid Dynamics Method", Journal of Aircraft, Vol. 26, No. 2, Dec. 1989, pp. 1105-1110.
- 3. Kramer, E., Hertel, J., and Wagner, S., "Euler Procedure for Calculation of the Steady Rotor Flow with Emphasis on Wake Evolution", AIAA Paper 90-3007, AIAA 8th Applied Aerodynamics Conference, August 1990, Portland, Oregon.
- 4. Chen, C.-L. and McCroskey, W. J., "Numerical Simulation of Helicopter Multi-Bladed Rotor Flow", AIAA Paper 88-0046, AIAA 26th Aerospace Sciences Meeting, January 1988, Reno, Nevada.
- 5. Srinivasan, G. R., Baeder, J. D., Obayashi, S., and McCroskey, W. J., "Flowfield of a Lifting Hovering Rotor A Navier-Stokes Simulation", Paper No. I.3.5, Proceedings of the Sixteenth European Rotorcraft Forum, Glasgow, Scotland, September 1990; also NASA TM 102862, August 1990.
- 6. Lorber, P. F., Stauter, R. C., and Landgrebe, A. J., "A Comprehensive Hover Test of the Airloads and Airflow on an Extensively Instrumented Model Helicopter Rotor", Proceedings of the 45th Annual Forum of the American Helicopter Society, Boston, Massachusetts, May 1989.
- 7. Duque, E. P. N., "A Numerical Analysis of the British Experimental Rotor Program Blade", NASA Technical Memorandum 102247, November 1989.
- 8. Srinivasan, G. R. and Baeder, J. D., "Recent Advances in Euler and Navier-Stokes Methods for Calculating Helicopter Rotor Aerodynamics and Acoustics", Proceedings of the Fourth International Symposium on Computational Fluid Dynamics, September 1991, Davis, California, pp. 1095-1100.

- 9. Pulliam, T. H. and Steger, J. L., "Implicit Finite-Difference Simulations of Three-Dimensional Compressible Flow", AIAA Journal, Vol. 18, 1980, pp. 159-167.
- 10. Srinivasan, G. R., Chyu, W. J., and Steger, J. L., "Computation of Simple Three-Dimensional Wing-Vortex Interaction in Transonic Flow", AIAA Paper 81-1206, AIAA 14th Fluid and Plasma Dynamics Conference, June 1981, Palo Alto, California.
- 11. Baldwin, B. S. and Lomax, H., "Thin Layer Approximation and Algebraic Model for Separated Turbulent Flow", AIAA Paper 78-0257, AIAA 16th Aerospace Sciences Meeting, January 1978, Huntsville, Alabama.
- 12. Srinivasan, G. R. and McCroskey, W. J., "Navier-Stokes Calculations of Hovering Rotor Flowfields", *Journal of Aircraft*, Vol. 25, No. 10, October 1988, pp. 865-874.

- 13. Wake, B. E. and Sankar, L. N., "Solutions of the Navier-Stokes Equations for the Flow About a Rotor Blade", *Journal of the American Helicopter Society*, Vol. 34, No. 2, April 1989, pp. 13-23.
- 14. Caradonna, F. X. and Tung, C., "Experimental and Analytical Studies of a Model Helicopter Rotor in Hover", NASA Technical Memorandum 81232, September 1981.
- 15. Srinivasan, G. R., McCroskey, W. J., Baeder, J. D., and Edwards, T. A., "Numerical Simulation of Tip Vortices of Wings in Subsonic and Transonic Flows", *AIAA Journal*, Vol. 26, No. 10, Oct. 1988, pp. 1153-1162.

Table 1
Calculated and Experimental Hover Performance Parameters for UH-60 Blackhawk and BERP Rotors for M_{tio}= 0.628

| Rotor | Methods of results | θ _c | C _T /σ | С_Q /σ | FM |
|--|----------------------------------|----------------|-------------------|-------------------------|------|
| | Experiments (Ref. 6) | Unknown | 0.085 | 0.0069 | 0.73 |
| UH-60 model rotor | N-S results | 9° | 0.084 | 0.0068 | 0.73 |
| | N-S results with new farfield BC | 9° | 0.087 | 0.0069 | 0.76 |
| UH-60 equivalent rectangular blade rotor | N-S results | 9° | 0.078 | 0.0065 | 0.68 |
| UH-60 linear twist blade rotor | N-S results | 9° | 0.071 | 0.0072 | 0.54 |
| UH-60 model rotor | N-S results | 13° | 0.140 | 0.0149 | 0.72 |
| | N-S results | 9° | 0.094 | 0.0098 | 0.68 |
| BERP rotor | N-S results | 13° | 0.168 | 0.0259 | 0.62 |



a) BERP rotor blade



b) UH60 Blackhawk rotor blade

Fig. 1 Planform views and surface grids for the UH60 and BERP rotor blades.

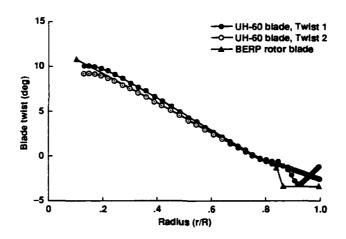


Fig. 2 Radial twist distributions for the UH60 and BERP rotor blades.

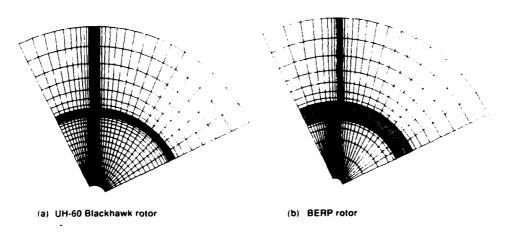


Fig. 3 Views of C-H grids in the plane of the blades; (a) UH60 blade, (b) BERP blade.

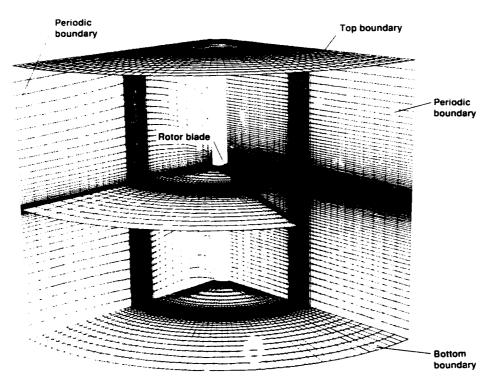


Fig. 4 View of C-H grid topology for a single BERP blade showing outer boundaries and grid in the plane of the blade.

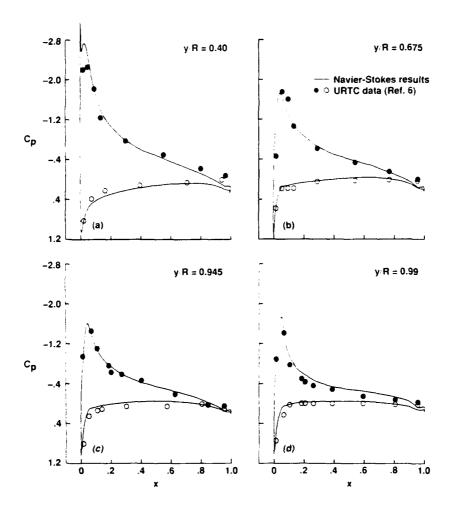


Fig. 5 Surface pressure distributions at various span stations for the UH60 blade compared with experimental data. $M_{tip} = 0.628$, Re = 2.75 x 10⁶, and calculated $C_T/\sigma = 0.084$.

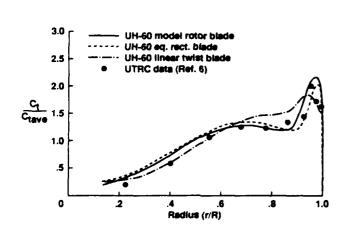


Fig. 6 Sectional thrust loading for the UH60 blade, equivalent UH60 rectangular blade, and the UH60 blade with linear twist distribution in the tip region. $M_{tip} = 0.628$, $\theta_c = 9^\circ$, and $Re = 2.75 \times 10^6$.

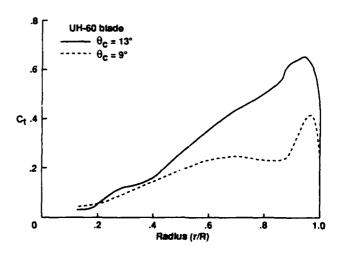


Fig. 7 Comparison of sectional thrust loading for the UH60 blade for two thrust conditions. $M_{tip} = 0.628$, and Re = 2.75×10^6 .

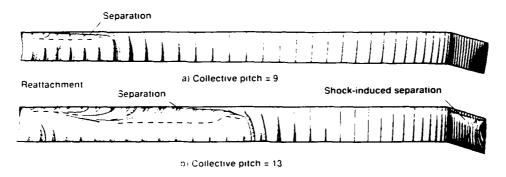


Fig. 8 Upper surface particle flow (skin friction) patterns of the UH60 blade for $\theta_c = 9^{\circ}$ and 13° cases at $M_{tip} = 0.628$ at Re = 2.75 x 10⁶.

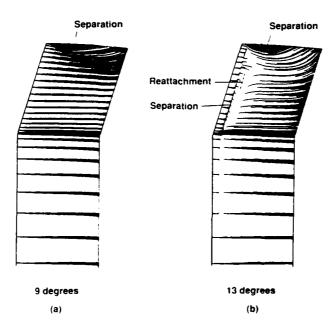


Fig. 9 Close-up view of surface particle flow in the tip region for the UH60 blade for $\theta_c=9^\circ$ and $\theta_c=13^\circ$ at $M_{tip}=0.628$, and Re = 2.75 x 10^6 .

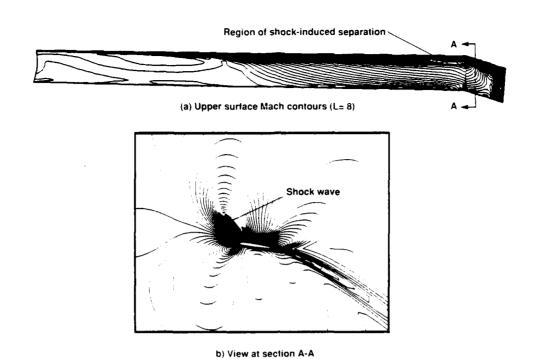


Fig. 10 Mach contours for the UH60 blade for the conditions of $M_{tip} = 0.628$, $\theta_c = 13^{\circ}$, and Re = 2.75 x 10^{6} . Views show a) upper surface contours at L = 8 (away from the wall), and b) cross-sectional plane at r/R = 0.94.

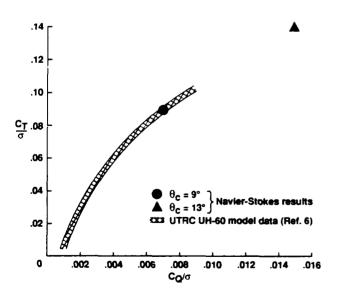


Fig. 11 Comparison of calculated and experimental hover performance for the UH60 model rotor.

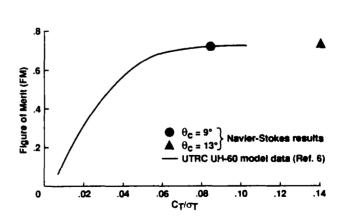


Fig. 12 Comparison of calculated and measured Figure of Merit for the UH60 model rotor.

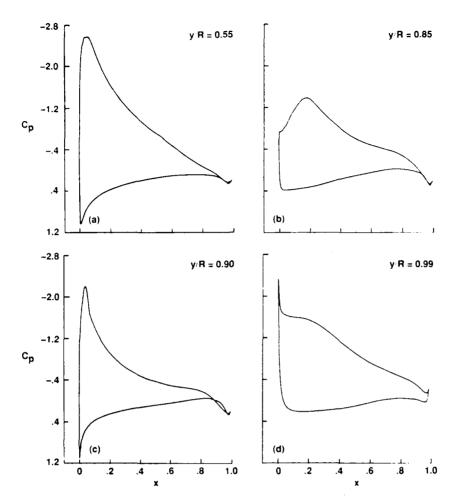


Fig. 13 Typical surface pressure distributions for the BERP rotor blade at different span stations; M_{tip}

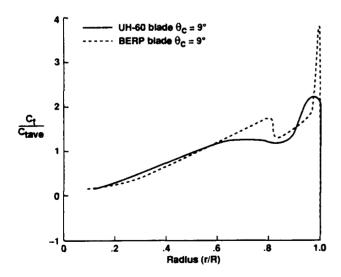


Fig. 14 Radial thrust loadings (based on local chord) for UH60 and BERP blades at the same collective pitch setting of $\theta_c = 9^{\circ}$ with $M_{tip} = 0.628$.

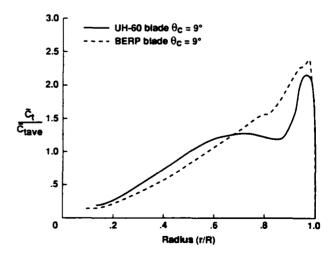


Fig. 15 Radial thrust loadings (based on equivalent chord) for UH60 and BERP blades at the same collective pitch setting of $\theta_c = 9^{\circ}$ with $M_{tip} = 0.628$.

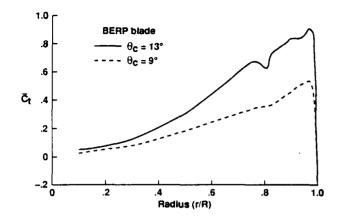


Fig. 16 Comparison of radial thrust loadings for BERP blade at $\theta_c=9^\circ$ and $\theta_c=13^\circ$ with $M_{tip}=0.628$ and Re = 2.94 x 10^6 .

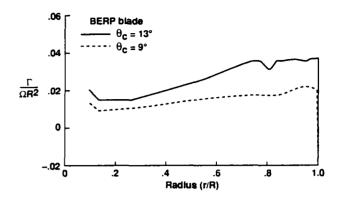


Fig. 17 Bound circulation distributions for BERP blade for the conditions of Fig. 16.

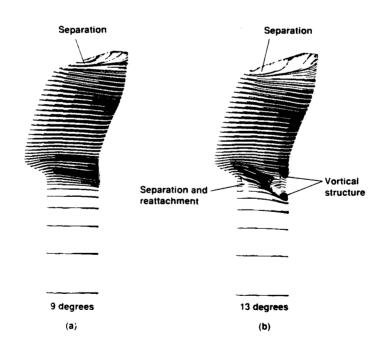


Fig. 18 Surface particle flow details mimicing oil flow patterns for the BERP blade at $\theta_c = 9^{\circ}$ and 13°; $M_{tip} = 0.628$ and Re = 2.94 x 10⁶.

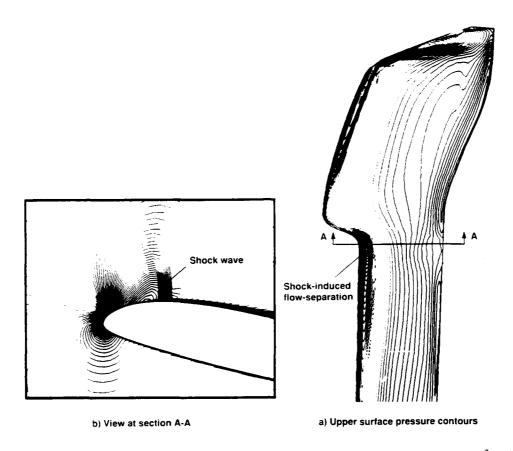


Fig. 19 Pressure contours of the BERP blade at $M_{tip} = 0.628$, $\theta_c = 13^{\circ}$, and Re = 2.95×10^{6} . Views show a) upper surface and b) cross-sectional plane at r/R = 0.80.

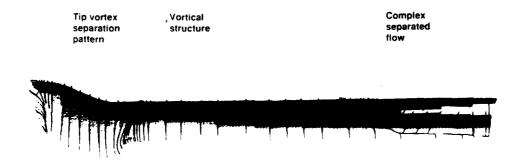


Fig. 20 Upper surface particle flow tracers pattern for the BERP blade at $M_{tip}=0.628,\,\theta_c=13^\circ,\,{\rm and}$ Re = 2.94 x 10⁶.

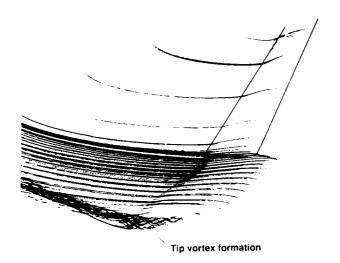


Fig. 21 Near-field view of tip vortex formation and roll-up process for the BERP blade at $\theta_c = 13^{\circ}$, $M_{tip} = 0.628$.

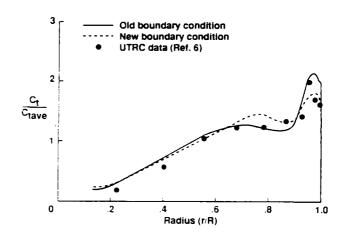


Fig. 22 Sectional thrust distributions for the UH60 blade with old and new farfield boundary conditions compared with experimental data. $M_{tip}=0.628,\,\theta_c=9^{\circ}$ and Re = 2.75 x 10^{6} .

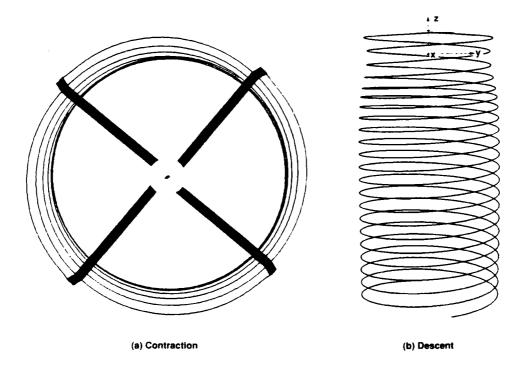


Fig. 23 Calculated tip vortex trajectory for a 4-bladed UH60 model rotor in hover showing wake contraction and descent; $M_{tip} = 0.628$, $\theta_c = 9.0^{\circ}$, Re = 2.75 x 10^{6} .

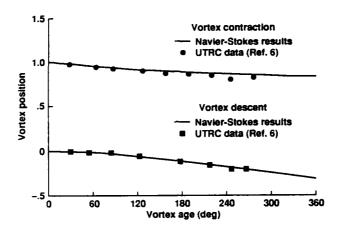


Fig. 24 Comparison of wake contraction and descent for a 4-bladed UH60 model rotor with experimental data for the conditions of Fig. 22.